Advanced Functional Materials

ADVANCED FUNCTIONAL MATERIALS
www.afm-journal.de

RESEARCH ARTICLE

Transcending Conventional Carbon Nitrides: Three-in-One Multi-Molecular Synergy Engineering in Covalent Heptazine Framework Unlocks Roust High-Rate Sodium-Ion Storage

Yanxin Yu[1] | Yufan Ren[1] | Yanbiao Ren[1] | Qianqian Jin[1] | Hailin Cong[1] | Shi Wang[2,4,3] | Zhong Jin[3]

[1]College of Chemistry, Chemical Engineering and Materials Science, Zaozhuang University, Zaozhuang, China | [2]State Key Laboratory of Flexible Electronics (LoFE), Institute of Advanced Materials (IAM), School of Chemistry and Life Sciences, Nanjing University of Posts & Telecommunications, Nanjing, China | [3]State Key Laboratory of Coordination Chemistry, MOE Key Laboratory of Mesoscopic Chemistry, MOE Key Laboratory of High Performance Polymer Materials and Technology, Jiangsu Key Laboratory of Green Energy Catalysis and Intelligent Chemical Engineering, Suzhou Key Laboratory of Green Intelligent Manufacturing of New Energy Materials and Devices, Tianchang New Materials and Energy Technologies Research Center, Institute of Green Chemistry and Engineering, School of Chemistry & Chemical Engineering, Nanjing University, Nanjing, China | [4]Key Laboratory of Functional Molecular Solids, Ministry of Education, Anhui Engineering Research Center of Carbon Neutrality, College of Chemistry and Materials Science, Anhui Normal University, Wuhu, China

Correspondence: Yanxin Yu (yanxinyu@uzz.edu.cn) | Hailin Cong (conghailin@sdut.edu.cn) | Shi Wang (iamshiwang@njupt.edu.cn) | Zhong Jin (zhongjin@nju.edu.cn)

Received: 4 November 2025 | **Revised:** 25 December 2025 | **Accepted:** 3 January 2026

Keywords: carbon nitrides | covalent heptazine framework | graphitic carbon nitride | sodium-ion batteries

ABSTRACT

Carbon nitrides (CNs), particularly graphitic carbon nitride (g-C_3N_4), show promise as electrodes for sodium-ion batteries (SIBs) due to exceptional stability and Na^+ storage potential. However, the low intrinsic conductivity and insufficient activity of CNs hamper the realization of both high capacity and high stability. Herein, this work proposes a multi-active-function modulation strategy to solve such challenges by integrating heptazine with functional conductive modules via active linkers, as exemplified by the rational design of a benzothiadiazole cooperated with alkynyl bifunctionalized covalent heptazine framework (BTA-CHF). This covalent linkage, via the alkynyl bridge, creates a fully electron-conductive skeleton densely packed with multiple Na^+-storage sites. Thus, as a SIBs anode, BTA-CHF renders record-high performance with exceptional capacity (912.1 mAh g^{-1} at 0.1 A g^{-1}), outstanding rate property (273.8 mAh g^{-1} at 10.0 A g^{-1}), and inspiring cyclability (~93.9% capacity sustainability through 20 000-cycles at 10 A g^{-1}). More impressively, the BTA-CHF//$Na_3V_2(PO_4)_3$ full battery exhibits a notable capacity of 836.8 mAh g^{-1} at 0.1 A g^{-1}, remarkable high-rate performance of 166.9 mAh g^{-1} at 10 A g^{-1}, and maintains 143.2 mAh g^{-1} after 1000 cycles at 10 A g^{-1}. This work demonstrates a novel approach to engineer advanced CNs electrodes for high-efficiency SIBs.

1 | Introduction

Sodium-ion batteries (SIBs) are emerging as a promising alternative to lithium-ion batteries (LIBs) due to the abundance of sodium resources and their cost-effectiveness, meeting the growing demand for portable devices [1–3]. In terms of the working mechanism, SIBs are very similar with LIBs [4, 5]. Thus, considerable research has been devoted to adapting the successful materials used in LIBs for SIBs [6–8]. However, anode materials such as graphite cannot be directly applied in SIBs because the Na^+ ion has a larger ionic radius than Li^+ [4, 9-12]. Other non-carbon choices, such as alloys and transition metal compounds,

are plagued with poor cyclability because of their huge volume deformation, leading to them being away from SIBs [13–16]. Therefore, it is crucial to explore highly efficient anode materials for SIBs.

Carbon nitrides (CNs), by virtue of porous defect-rich structure and high-nitrogen content, have attracted considerable attention as electrode candidates for SIBs [17–21]. Among CNs, research has primarily focused on graphitic carbon nitride (g-C_3N_4) [22]. Theoretical research confirms that g-C_3N_4 possesses a Li^+ storage capacity of 524 mAh g^{-1}, thus implying its potential for Na^+ storage [23]. However, g-C_3N_4 exhibits low reversible capacity and inadequate cycling stability in SIBs due to the intrinsic issues of CNs: poor conductivity, chemical inertness, and an irreversible Na^+ intercalation mechanism [24, 25]. To date, many strategies such as heteroatom doping and composite formation have been tried to modulate its features. Unfortunately, these have yielded only partial improvements in Na^+-storage performance [26–29]. While heteroatom doping can enhance charge transport by creating surface defect through the substitution of carbon atoms with metal or non-metal atoms in g-C_3N_4, it still suffer from poor reversible capacity caused by the irreversible intercalation mechanism [30]. Although composite technology enhances the specific capacity compared to pure g-C_3N_4, the rate capability remains unsatisfactory due to poor interfacial contact between g-C_3N_4 and the added components [31]. More poorly, g-C_3N_4 frequently acts only as a substrate in composites, while complexes contribute to more capacity [32, 33]. Namely, these strategies fail to effectively modulate the electronic structure of g-C_3N_4, which is the fundamental limitation underlying its poor Na^+-storage performance. To date, the development of novel CNs beyond g-C_3N_4 for high-efficiency SIBs remains highly challenging.

In fact, little attention has been focused on chemical structure modification, which can precisely tailor the intrinsic electronic features of CNs framework with totally new physicochemical properties for Na^+-storage. The fundamental limitation of CNs lies in their intrinsic defects, where heptazine motifs are predominantly interconnected through electronically insulating tertiary N-nodes. This critical flaw severs the essential π-conjugation pathways across the network and limits the availability of efficient redox-active sites, thereby severely impairing both charge transport and Na^+-storage capacity. Replacing these insulating tertiary N-nodes with functional π-electron modules could establish continuous conjugation across the network while introducing multiple active sites, thereby enhancing both conductivity and Na^+-storage performance.

Based on these considerations, this work proposes a "three-in-one" synergistic strategy that integrates multiple active modules to construct novel CNs for high-efficiency SIBs, and a benzothiadiazole coordinated with alkynyl motifs modulated covalent heptazine framework (BTA-CHF) as proof-of-concept is designed (Scheme 1). In BTA-CHF, the active alkynyl groups serve as bridges, conjugating the benzothiadiazole and heptazine cores into a periodic structure. This enhances both electron conduction and Na^+-storage performance. The theoretical evaluations suggest that the centers of heptazine, benzothiadiazole, and alkynyl can not only strongly increase the conductivity but also dedicate as plentiful redox-active sites for Na^+-storage, and thereby exhibiting an unheard theoretical specific capacity as 920.0 mAh g^{-1}. More importantly, the deeply extended conjugation across the benzothiadiazole-alkynyl-heptazine framework reduces the bandgap of BTA-CHF to 1.60 eV, indicating enhanced electronic conductivity. Thus, SIBs assembled with BTA-CHF anode validate record-high performance with heartening reversible capacity (912.1 mAh g^{-1} under 0.1 A g^{-1}), high-rate property (273.8 mAh g^{-1} under 10.0 A g^{-1}), and impressive cyclability with less than 7% decay undergoing 20 000-cycles under 10.0 A g^{-1}. More impressively, the BTA-CHF//$Na_3V_2(PO_4)_3$ full battery exhibits a notable reversible capacity of 836.8 mAh g^{-1} at 0.1 A g^{-1}, remarkable high-rate performance of 166.9 mAh g^{-1} at 10 A g^{-1}, and sustains 143.2 mAh g^{-1} after 1000 cycles at 10 A g^{-1}. This work opens a new avenue for developing high-performance CN-based electrodes for SIBs.

2 | Results and Discussion

2.1 | Design and Theoretical Prediction

Our interest in BTA-CHF stems from its unique structure: a fully conjugated periodic framework featuring numerous multi-active centers. This design promises simultaneous enhancement of Na^+-storage capacity and electronic conductivity for efficient SIBs. The Na^+-storage potential of BTA-CHF was evaluated by a systematic preceding density functional theory (DFT) calculations. First, the Na^+-storage centers of BTA-CHF were identified by molecular electrostatic potential (MESP) simulations, in which blue means the negative and red represents the positive. As described in Figure 1a, the MSEP result suggested that the blue area is primarily distributed heptazine, alkynyl, and benzothiadiazole cores and simultaneously at the molecule edge of the BTA-CHF sample. The charge distribution of BTA-CHF shows that it's facile to interact with positively charged Na^+, which could considerably shorten the diffusion path and improves efficiency of redox reaction. Consequently, each heptazine core, alkynyl unit, and benzothiadiazole core can theoretically interact with 6, 2, and 2 Na^+, respectively, yielding a theoretical reversible capacity of 920.0 mAh g^{-1}. Furthermore, the electron band structure and density of state (DOS) of BTA-CHF were analyzed to assess its charge transport properties. The electron mobility was evaluated based on the bandgap, in particular the energy separation between valence band maximum (VBM) and conduction band minimum (CBM). As shown by the VBM in Figure 1b, the electron density of BTA-CHF exhibits a nearly homogeneous distribution across the entire framework. This results from the fully extended π-conjugation formed via alkynyl bridges that link heptazine and benzothiadiazole units in the periodic structure. In the CBM of BTA-CHF, only a small fraction of electron charge resides on the N-atoms of the heptazine rings, while the majority is concentrated on the benzothiadiazole and alkynyl moieties (Figure 1c). Comparatively, g-C_3N_4 does not have such electronic features around its whole structure, while the high electron density floods in both VBM and CBM of the isolated heptazine cores through tertiary-N nodes (Figure S1). The distinct electron density distribution in BTA-CHF, compared to g-C_3N_4, reveals its superior capability for charge capture and transport. This enhancement is attributed to the synergistic effect between the benzothiadiazole and alkynyl functional centers. As

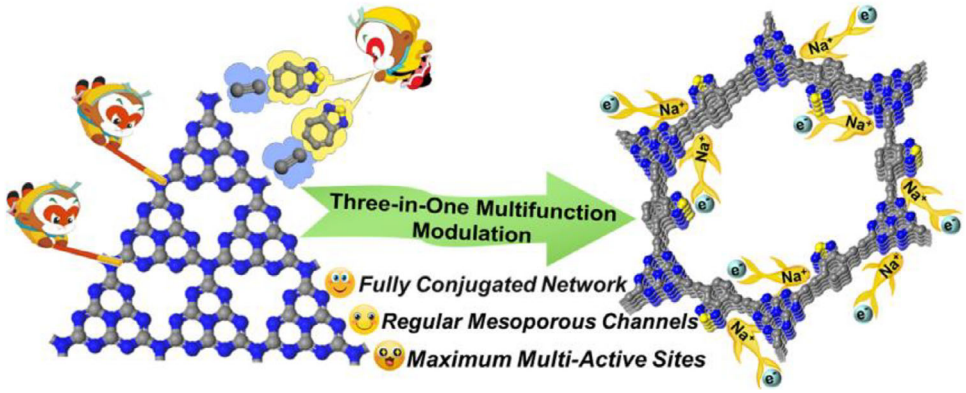

SCHEME 1 | Schematic illustrating the "three-in-one" multi-function synergistic modulation strategy to construct novel CNs for efficient Na^+-storage, and the design of benzothiadiazole cooperated with alkynyl functionalized covalent heptazine framework (BTA-CHF) as the first concept-of-proof.

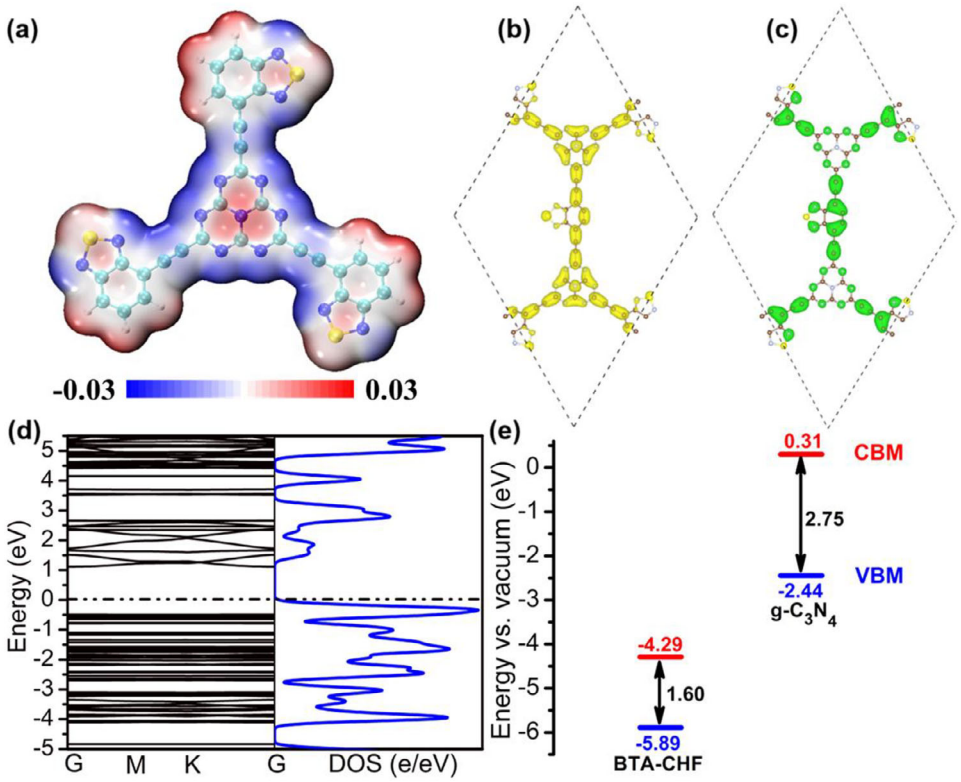

FIGURE 1 | Schematic diagram of the pre-theoretical calculation for BTA-CHF: (a) The molecular electrostatic potential simulation. (b) The valence band maximum. (c) The conduction band minimum. (d) Band structures and density of states. (e) Band alignment of BTA-CHF and g-C_3N_4.

depicted in the DOS of BTA-CHF (Figure 1d), it has a higher dispersion degree on electron density of CBM over VBM than that of g-C_3N_4 (Figure S2), suggesting the more efficient charge migration of BTA-CHF. In terms of energy gap (Figure 1e), g-C_3N_4 has a large level as 2.75 eV, while BTA-CHF displays a remarkably reduced value to 1.60 eV through its band structure and correlative projected density of states (Figure S3). This is attributed to the extended conjugation along the heptazine-alkynyl-benzothiadiazole backbone in the periodic framework, which leads to improved charge transport conductivity. Notably, the lower CBM of BTA-CHF compared to g-C_3N_4 demonstrates stronger electron avidity of BTA-CHF, which is easier to trap more electron for reduction reaction, and then obtain delightful specific capacity [34]. Moreover, the lower VBM of BTA-CHF compared to that of g-C_3N_4 implies the formation of more stable charged intermediates. This facilitates faster reaction kinetics, thus contributing to excellent rate capability and long-term cycling stability [35]. Collectively, these results validate that our design concept in novel CNs by multi-active modules synergistic modulation would realize multiple Na^+-storage sites and especially tailored natural electronic features for high-efficiency SIBs.

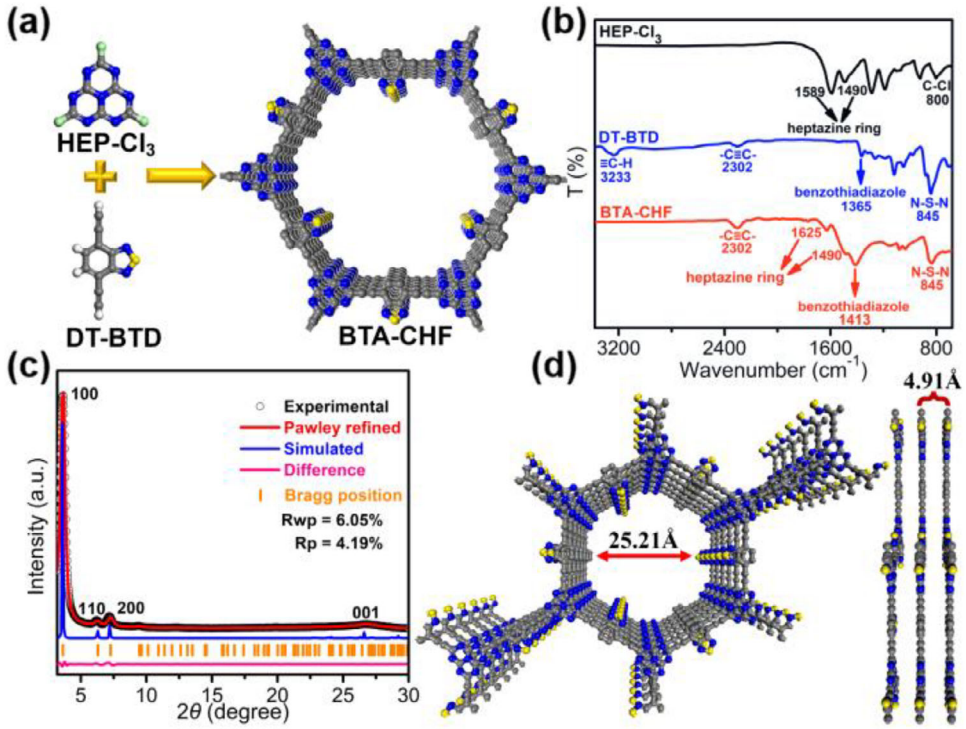

FIGURE 2 | Synthesis and structure characterization of BTA-CHF. (a) The schematic diagram of the synthesis of BTA-CHF. (b) FT-IR spectra of HEP-Cl_3, DT-BTD, and BTA-CHF. (c) Experimental and refined PXRD curves of BTA-CHF. (d) The top and side views of simulate BTA-CHF model based on the AA-stacking. (For FT-IR and PXRD, each sample was measured three times).

2.2 | Preparation and Characterizations

Inspired by these DFT evaluation results of attractive electronic properties and extraordinary theoretical specific capacity, we prepared this BTA-CHF via an adept one-step reaction between 2,5,8-triclo-s-heptazine (HEP-Cl_3) and 4,7-diethynyl 2,1,3-benzothiadiazole (DT-BTD) based on a normal solvothermal reaction (Figure 2a). The successful formation of chemical bonds was first corroborated using the Fourier transform infrared (FT-IR) spectroscopy. As shown in Figure 2b, the FT-IR spectrum displays that BTA-CHF contains heptazine, benzothiadiazole, and alkynel modules. For HEP-Cl_3, the characteristic signal at 800 cm^{-1} belongs to C–Cl stretching vibration, and two signals at 1589 and 1490 cm^{-1} are induced by C═N stretching vibration and heptazine-skeleton vibration, respectively. In the FT-IR spectrum of DT-BTD, the distinctive signals at 3233, 2302, 1365, and 845 cm^{-1} are indicative of ≡C—H, —C≡C—, C═N (benzothiadiazole), and N–S–N stretching vibration, respectively. For the BTA-CHF product, the signal of C—Cl as well as ≡C—H has disappeared, while the peak of —C≡C— is retained with enhanced signal intensity, indicating the successful condensation between C—Cl and ≡C—H groups. Besides, C═N characters at 1589 cm^{-1} (heptazine core) and 1365 cm^{-1} (benzothiadiazole unit) move to the high wavenumber region of 1625 and 1413 cm^{-1}, which is due to the enhanced conjugation and meanwhile presents stronger evidence for the perfect occurrence of such condensation reaction. The crystalline feature of BTA-CHF was further confirmed via powder X-ray diffraction (PXRD) analysis, showing a sharp diffraction signal belonged to the (100) facet at 3.65° (Figure 2c). Other relatively weaker peaks assigning to (110) and (200) planes are located at 6.30° and 7.28°, respectively. Especially, the diffraction peak at 26.6° with a broad facet (001) is caused by the strong interlayer π–π interaction [36, 37]. The 2D layer framework of BTA-CHF was refined using AA stacking model, followed by Pawley refinement within PM6 space group (Figure S4 and Table S1), showing that its experimental PXRD result well matches the theoretical model with $R_{wp} = 6.05\%$ and $R_p = 4.19\%$. In comparison, there is a significant difference between the PXRD patterns based on its staggered AB-stacking model and the experimental PXRD peaks (Figure S5).

The porosity feature of BTA-CHF was further confirmed by N_2 adsorption-desorption testing was carried out. The mesoporous characteristics were confirmed by the type IV isotherms with the specific surface area as 39.2 $m^2\ g^{-1}$ (Figure S6). Despite its low surface area, BTA-CHF exhibits exceptional electrochemical performance. This suggests that Na^+ storage is governed by chemisorption rather than simple physisorption. The pore size distribution shows an average diameter ~2.52 nm (Figure S7), which matches well with the near-circular channels of BTA-CHF in the simulated model (Figure 2d). Such pore channel can realize the efficient transfer of electrolyte species in the process of discharge/charge.

The BTA-CHF with a stick-shaped appearance was revealed through scanning electron microscope (SEM) images (Figure S8). Its high-resolution transmission electron microscope (HRTEM) image of BTA-CHF displays distinct local crystal structure with a stacking distance about 0.49 nm (Figure S9), which is almost consistent with that of its theoretical model (Figure 2d), confirming its stacked lamellar skeleton. Notably, this domain crystallization implies the facilitated ion mobility since the presence of

amorphization can effectively reduce blocking effect caused by the intensive lattice framework on the charge transmission [38]. Consequently, efficient electron transfer in BTA-CHF is achieved, owing to its dual structural features: an extended π-conjugated framework and localized crystalline domains. Finally, the thermogravimetric analysis (TGA) revealed that BTA-CHF can keep outstanding structural stability up to 400°C without noticeable weight loss (Figure S10), showing its robust skeleton owing to strong multi-component blocks for the application in SIBs.

2.3 | Electrochemical Performance of BTA-CHF

The abundant multi-redox-active centers (heptazine, alkynyl, and benzothiadiazole) integrated into the fully π-conjugated network underscore the potential of BTA-CHF as a high-performance anode for SIBs. Therefore, its electrochemical performance was investigated in coin (CR2032) cell with the cutoff voltage of 0.01–3.0 V. First, the sodiation/desodiation behavior of BTA-CHF was probed by cyclic voltammetry (CV) measurements at 1.0 mV s^{-1}. As shown in Figure 3a, the cathodic signal located at 0.59 V (first cycle cathodic scan) can be ascribed to irreversible sodiation caused by solid electrochemical interface (SEI) [39]. Three cathodic/anodic peak pairs of 1.60/0.43, 1.05/1.61, and 0.44/2.11 V could be attributed to the sodiation/desodiation behavior produced at heptazine, benzothiadiazole, and alkynyl cores, respectively. These redox behaviors confirm the multiple Na^+ intercalation process at active centers of BTA-CHF and reveal the practical contribution of heptazine core for Na^+-storage. The near-perfect overlap between the second and third cycle curves demonstrates the excellent reversibility and cyclability of study BTA-CHF for Na^+-storage. In contrast, the CV curves of g-C_3N_4 displays rather weak feeble sodiation/desodiation behavior, suggesting its insufficient reversibility as well as cyclability (Figure S11). This further confirms that triggering the Na^+-storage activity of heptazine units is crucial for developing high-performance CN-based SIB electrodes. As can be seen from Figure 3b, BTA-CHF delivered initial capacities of 2442.8 mAh g^{-1} (discharge) 1271.0 mAh g^{-1} (charge), yielding a moderate Coulombic efficiency (CE) of 52.0% (Figure 3b). The discharge capacity initially decays before stabilizing at a reversible value of 912.1 mAh g^{-1} after the first six cycles. This phenomenon results from the formation of SEI and the extensive electrolyte decomposition on the surface of electrode materials, which normally happens in the stage of the original cycles. Notably, the galvanostatic profiles exhibit sloping charge/discharge curves without distinct plateaus. This originates from strong electronic coupling between adjacent redox-active centers, which causes a continuous shift in redox potential [40]. Furthermore, the rate capability of BTA-CHF exhibits discharge capacities as 880.9/0.2, 758.6/0.5, 654.1/1.0, 536.0/2.0, and 407.1/5.0 mAh g^{-1}/A g^{-1}, respectively (Figure 3c and Figure S12). Surprisingly, BTA-CHF demonstrated a record-high reversible capacity of 273.8 mAh g^{-1} at 10.0 A g^{-1}. Notably, fluctuations in the Coulombic efficiency are observed during cycling. In the initial cycles, this is attributed to the activation process of the BTA-CHF. In subsequent cycles, the efficiency variations are caused by voltage drops resulting from changes in the current density. When returned to 0.1 A g^{-1}, BTA-CHF recovers a capacity comparable to its initial stable value. More impressively, its maintains a specific capacity of 257.0 mAh g^{-1} at 10.0 A g^{-1} even after 20 000-cycles with ~93.9% capacity retention (Figure 3d), showing its extraordinary stability. Especially, the CE of BTA-CHF has been stable at 100%, emphasizing its high degree of reversible sodiation/desodiation process. More importantly, the electrochemical performance of BTA-CHF closely matches the theoretical predictions. In stark contrast, the g-C_3N_4 electrode only possessed 70.3 mAh g^{-1} while the current density creased to 1.0 A g^{-1} (Figure S13). More badly, the g-C_3N_4 electrode also exhibited poor cyclic stability (Figures S14 and S15). This strongly demonstrates the validity of the "three-in-one" multi-functional synergistic strategy for designing advanced CN electrodes in high-performance SIBs. Inspiringly, the high-performance of BTA-CHF not only surpasses that of g-C_3N_4-derived materials, but also represents the top value compared to such electrodes relying on the redox-active units (Figure 3e and Table S2).

The charge transport impedance of BTA-CHF was further characterized by electrochemical impedance spectroscopy (EIS). As a result, its impedance shows an obvious decline from 118.3 to 81.3 Ω after five cycles (Figure S16), highlighting the significant enhancement of electrode kinetics for BTA-CHF and its facilitated transfer of Na^+/e^-. Notably, BTA-CHF exhibits a significantly lower impedance than g-C_3N_4 (Figure S17), thus confirming its superior electrical conductivity. Additionally, the galvanostatic intermittent titration technique (GITT) was utilized to characterize ionic diffusion within BTA-CHF [41]. Markedly, obvious peaks can be observed from the diffusion coefficient curves (Figures S18 and S19), reflecting the Na^+ insertion into active sites during the electrochemical cycling. The Na^+ diffusion coefficient of BAT-CHF is calculated as $10^{-6.5}$–$10^{-8.4}$ cm^2 S^{-1}, which is super-outstanding compared to g-C_3N_4 (ranged between $10^{-14.5}$ and 10^{-17} cm^2 S^{-1}, Figures S20 and S21). These results corroborate the enhanced Na^+/e^- transport in BTA-CHF, afforded by its fully extended conjugated framework. To probe its electrochemical kinetics, CV measurements were performed at scan rates ranging from 0.2 to 1.0 mV s^{-1} (Figure S22). The continuous shift of the redox peaks with increasing scan rate indicates the highly reversible Na^+ storage behavior of BTA-CHF. The electrochemical kinetics of BTA-CHF were assessed by analyzing the peak current (i)-scan rate (v) relationship ($\log i = b \log v + \log a$). As is commonly understand that the b-value approaching 0.5 signifies diffusion-dependent charge storage, and it near 1 indicates capacitive-dominated process. The b-values are determined as 0.66/0.91 and 0.73/0.61 for the representative two cathodic/anodic peak pairs of 1.60/0.43 and 1.05/1.61 V (Figure 3f), which strongly suggests that the Na^+-storage of BTA-CHF is a fast capacitive-dominated process. This performance originates from the abundant, accessible multi-active centers embedded within the regular channels of BTA-CHF, which are supported by its fully conjugated skeleton. For the Na^+-storage of BTA-CHF, the capacitive contribution exhibits the highest value as 71.5% (1.0 mV s^{-1}), and decreases progressively to 34.3% at 0.2 mV s^{-1} (Figure 3g and Figure S23). The coexistence of capacitive and diffusion-controlled processes in BTA-CHF confirms its pseudocapacitive nature, which imparts significant advantages for energy storage. To further evaluate the practical ability of BTA-CHF as the anode material for SIBs, we assembled full cells pairing $Na_3V_2(PO_4)_3$ as the cathode. Before the full cells assembly, the BTA-CHF anode presodiation using sodium metal foil as the counter electrode in the half-cell system. Delightfully, the BTA-CHF//$Na_3V_2(PO_4)_3$ full cell exhibits a notable reversible

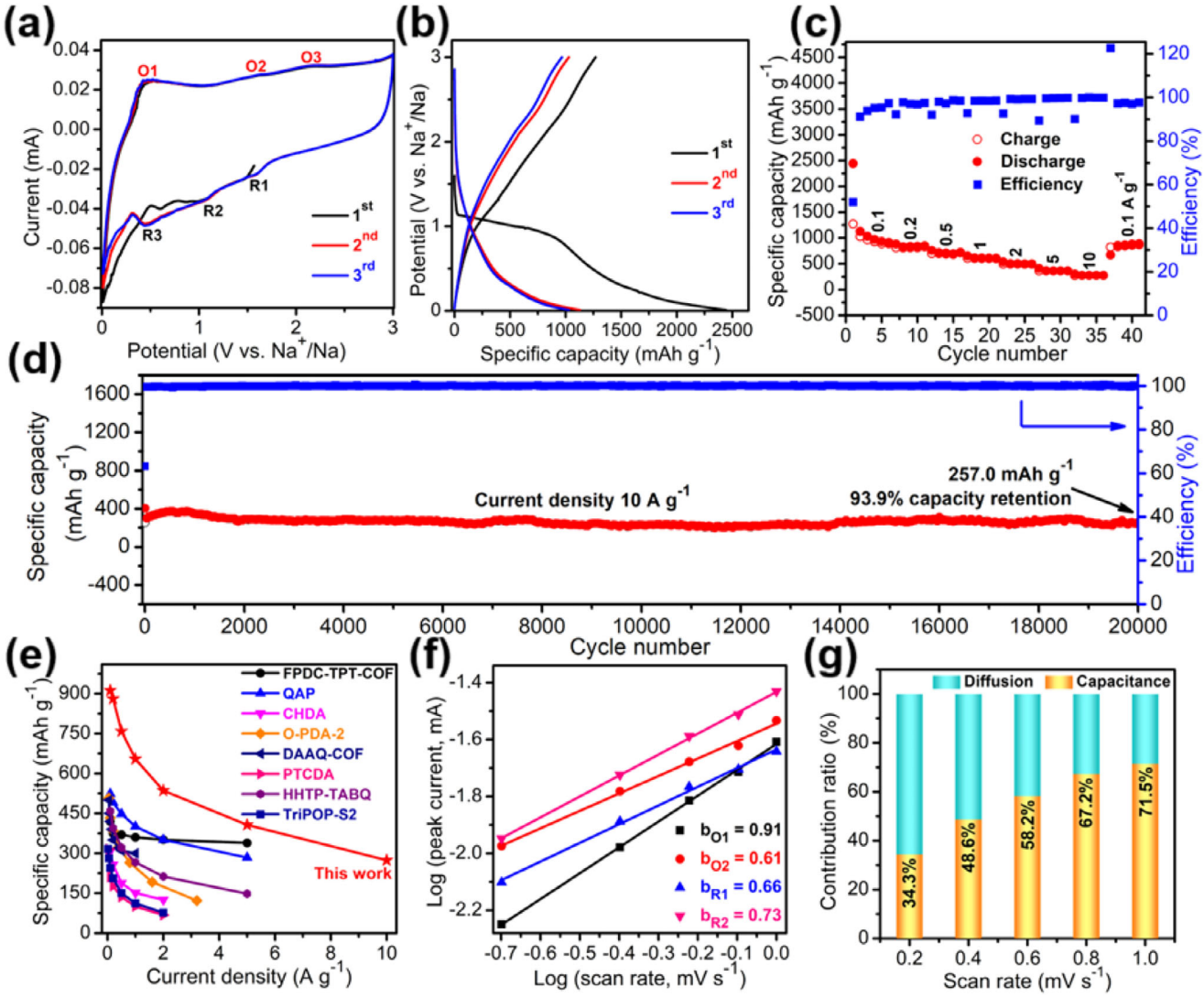

FIGURE 3 | A series of electrochemical performance of BTA-CHF: (a) CV curves of the original three cycles at the scan rate of 1.0 mV s^{-1}. (b) The discharge/charge curves of the original three cycles under the current density of 0.1 A g^{-1}. (c) The rate performance of the current density ranged from 0.1 to 10.0 A g^{-1}. (d) The long-cycling performance under the current density of 10.0 A g^{-1}. (e) The performance comparison between BTA-CHF and other electrodes relied on redox-active sites. (f) The b-value of the representative two cathodic/anodic peak pairs. (g) The contribution ration of the capacitive-dominant diffusion process in the scan rate ranged from 0.2 to 1.0 mV s^{-1}. (Each of these electrochemical properties was tested in three parallel experiments to eliminate outliers).

capacity of 836.8 mAh g^{-1} at 0.1 A g^{-1} and remarkable high-rate performance of 166.9 mAh g^{-1} even at 10 A g^{-1} (Figure S24). More impressively, the BTA-CHF//$Na_3V_2(PO_4)_3$ full cell maintains a high capacity of 143.2 mAh g^{-1} after 1000 cycles at 10 A g^{-1} (Figure S25). This result demonstrates the promise of BTA-CHF as a robust, high-rate anode material for SIBs.

2.4 | Na^+-storage Mechanism of BTA-CHF

To obtain an in-depth insight about the Na^+-storage of BTA-CHF electrode, FT-IR testing was first conducted to monitor the change of redox-active centers and assess their evolution during the different stages of charge/discharge process (Figure 4a,b). Prior to Na^+-storage, distinct vibrational signals appear at 1625 cm^{-1} (C═N of heptazine) and 1413 cm^{-1} (C═N of benzothiadiazole), 1490 cm^{-1} (heptazine skeleton), and 2302 cm^{-1} (C≡C). Upon discharging to 0.01 V, the detected signals for these peaks exhibits progressive attenuation until near-complete disappearance, verifying the efficient Na^+ insertion into these redox-active groups.

Upon charging to 3.0 V, these characteristic peaks progressively reappeared and restored to their original intensity, confirming the highly reversible and synergistic operation of the multi-active centers during sodiation/desodiation process. Even undergoing 20 000-cycles at 10.0 A g^{-1}, the FT-IR signature of BTA-CHF keeps almost identical (Figure S26), strongly indicating its outstanding electrochemical robustness.

To further monitor the evolution of redox-active centers during sodiation/desodiation, X-ray photoelectron spectroscopy (XPS) was employed on BTA-CHF. The initial BTA-CHF sample for XPS analysis was soaked overnight in electrolyte. Analysis of

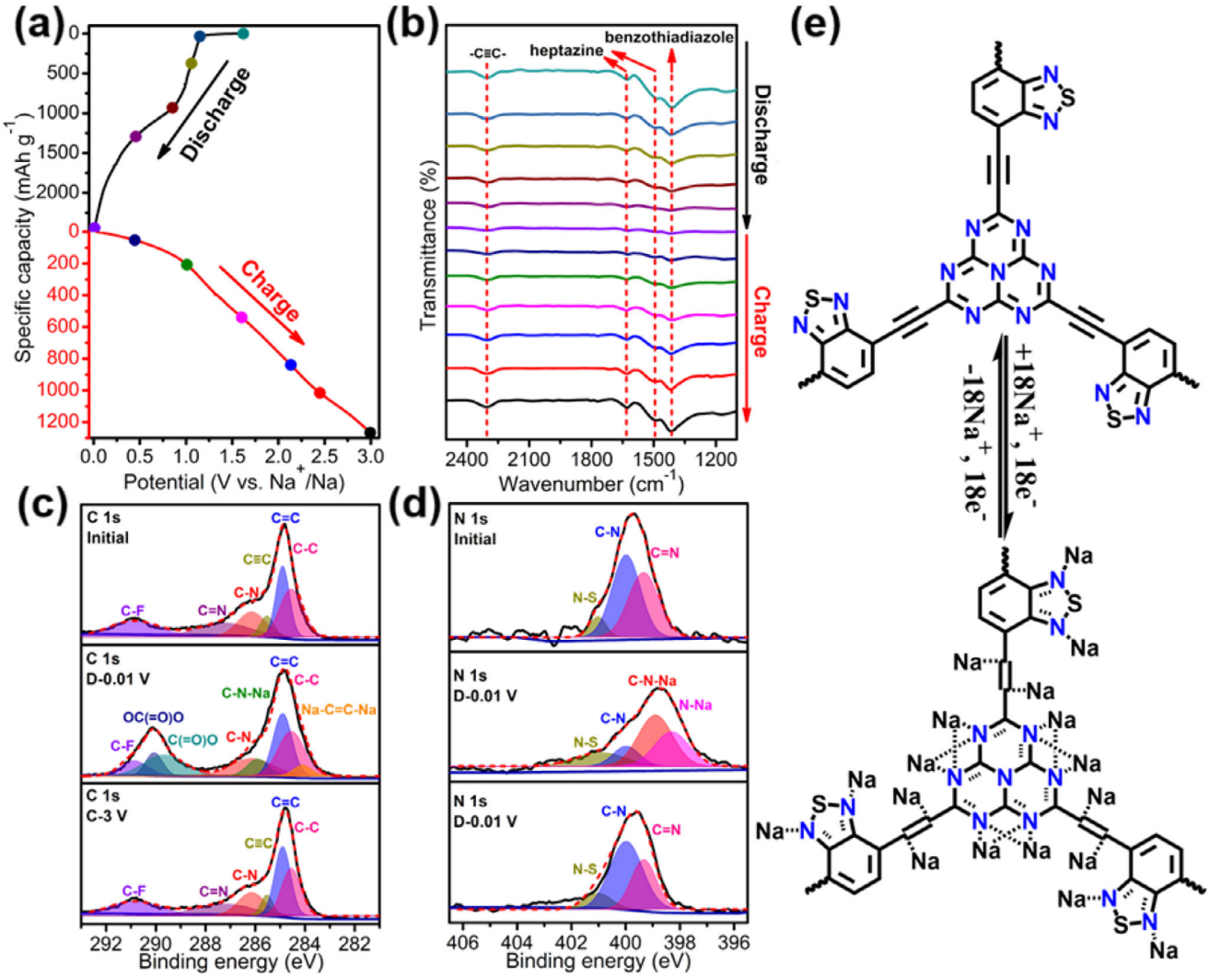

FIGURE 4 | Sodiation/desodiation mechanism of BTA-CHF by structural evolution: (a) The discharge and charge curves of BTA-CHF under the current density of 0.1 A g^{-1}. (b) The recorded FT-IR spectra at different voltage point during the discharge/charge process in (a). (c,d) C 1s and N 1s XPS spectra of BTA-CHF at different sodiation/desodiation states. (e) Schematic diagram of the confirmed sodiation/desodiation mechanism of BTA-CHF. (FTIR and XPS characterization for mechanism was achieved from two cells at identical states).

high-resolution C 1s XPS spectra of initial BTA-CHF (Figure 4c), distinct peaks locates at 284.55 eV (C—C, sp^3), 284.9 eV (C═C, sp^2), 285.53 eV (C≡C, sp), 286.15 eV (C—N), 287.27 eV (C═N), and 290.87 eV (C–F, which originates from electrolyte component). Following discharge to 0.01 V, the 287.27 eV (C═N) and 285.53 eV (C≡C) XPS peaks disappeared while notable peaks emerged at 284.1 eV (Na–C = C–Na) and 285.9 eV (C–N–Na), confirming the efficient sodiation of redox-active groups. It is worth noting that each C≡C unit only occurred two-electron redox reaction in BTA-CHF, which could be due to the strong inductive and steric-hindrance effect of Na–C = C–Na. The additional peaks that located at 290.06 and 289.67 eV can be belonged to OC(=O)O and C(=O)O groups, which are caused by the electrolyte decomposition in the stage of initial sodiation process. After recharging to 3.0 V, the signal change of these redox-active sites performed the opposite tendency and were almost comparable to those before sodiation. Similarly, the reversible changes in the N 1s XPS peaks serve as compelling evidence for Na^+ storage at the redox-active sites (Figure 4d). From the N 1s spectra of pristine BTA-CHF, three peaks at 399.33 eV (C═N), 399.98 eV (C–N), and 401.02 eV (N–S) can be distinctively observed. Upon discharge to 0.01 V, the C = N peak vanished and C–N signal intensity weakened with the concomitant emergence at 398.9 eV (C–N–Na) and 398.3 eV (N–Na). In addition, the signal of N-S moved to 400.92 eV from 401.02 eV, which is mainly due the electron-donor effect of sodium. Expectedly, all these peaks of active units can be reproduced after recharging to 3.0 V. Both FT-IR and XPS data confirm the efficient and nearly synchronous involvement of multiple redox-active centers throughout the sodiation/desodiation process. Together, these results converge to support the Na^+-storage mechanism for BTA-CHF illustrated in Figure 4e.

2.5 | Theoretical Study for Na^+-Storage of BTA-CHF

To elucidate the redox mechanism, DFT calculations were conducted to probe the multi-active centers of BTA-CHF during sodiation/desodiation. The total energy of each cell is employed

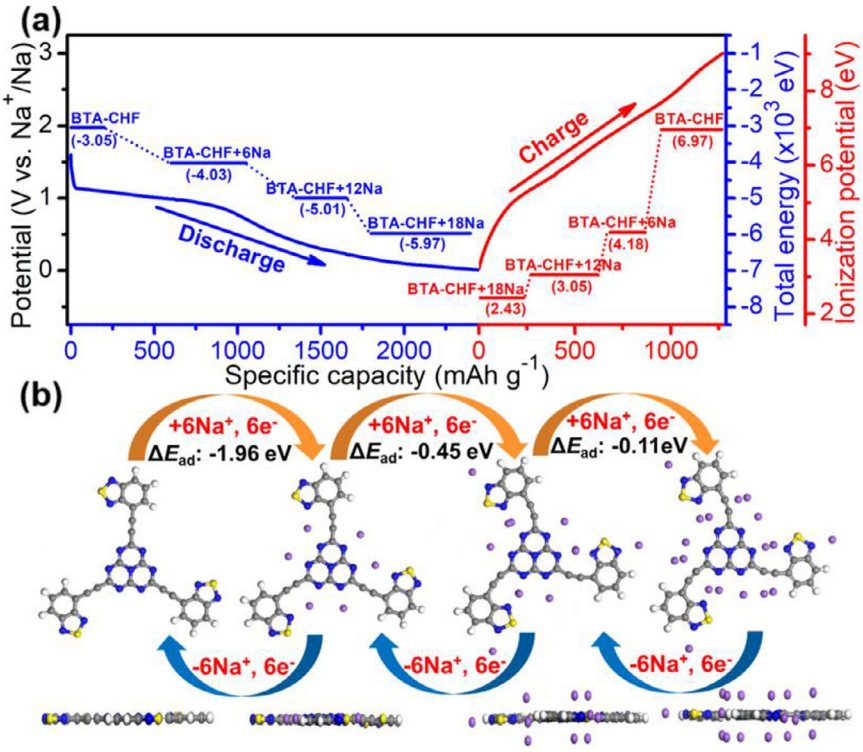

FIGURE 5 | Theoretical study of sodiation/desodiation mechanism of BTA-CHF: (a) The proposed sodiation/desodiation route of BTA-CHF. (b) The structure assessment of BTA-CHF during sodiation/desodiation process.

to evaluate activity strength in the sodiation process, and determined as -3.05×10^3, -4.03×10^3, -5.01×10^3, and -5.97×10^3 eV for BTA-CHF, BTA-CHF+6Na, BTA-CHF+12Na, and BTA-CHF+18Na, respectively. Computationally, there is a difference as -0.98×10^3 eV between BTA-CHF and BTA-CHF+6Na, which originates from each heptazine core reacts with six Na-atoms in BTA-CHF. In addition, the total energy of BTA-CHF+6Na based on the heptazine core is lower than that based on benzothiadiazole core (-3.99×10^3 eV), suggesting that heptazine preferentially reacts with Na^+ in BTA-CHF. A comparative analysis indicates that Na^+ has a higher affinity for the benzothiadiazole core compared to the alkynyl motifs. During the process of desodiation, the ionization energy are determined as 2.43, 3.05, 4.18, and 6.97 eV for BTA-CHF+18Na, BTA-CHF+12Na, BTA-CHF+6Na, and BTA-CHF unit, respectively. Apparently, BTA-CHF+18Na possesses the lowest value of ionization energy, indicating it readily relieves six Na^+ from one heptazine core to convert to BTA-CHF+12Na, and sequentially releases six Na^+ in each of the three benzothiadiazole cores and the three alkynyl units to recreate BTA-CHF. This evidence confirms that the heptazine core's reactivity toward Na^+ is fully activated in BTA-CHF. This activation is achieved by customizing its intrinsic electronic structure through the synergistic modification with benzothiadiazole and alkynyl units. Then, the optimal geometries of Na atoms located at different active sites in BTA-CHF were further achieved through simulations, and the adsorption energy (ΔE_{ad}) was utilized to evaluate the binding spontaneity of Na atom on BTA-CHF (Figure 5b). Combined with the MSEP result, it can be easily found that the vicinity of C = N sites of heptazine center performs the most negative status and readily obtains 6Na atoms with the ΔE_{ad} as −1.96 eV in each unit, highlighting its strongest reactivity for Na^+ owing to the stronger electronegativity of N atom than other active centers. Then, the active C=N site of benzothiadiazole cores display a second negative state and can accept 2Na with the ΔE_{ad} as −0.45 eV in each benzothiadiazole unit. Finally, the vicinity near C≡C bands exhibits a relatively low negative level via the entire conjugated skeleton. Each C≡C site can firmly accepted 2Na atoms with the ΔE_{ad} of −0.11 eV through optimization. Once introducing more than 2Na atoms into every C≡C site, the robust planar structure of BTA-CHF would be devastatingly destructed and the next adsorption potential could also be impacted (Figure S27). The severe distortion of the C≡C units upon 4Na coordination manifests the strong inductive and steric effects of the Na–C = C–Na adduct, facilitating its reorganization into a 2Na–C–C–2Na structure. The efficient operation of multi-active centers (heptazine, alkynyl, and benzothiadiazole) in BTA-CHF enables record-high Na^+- storage, evidenced by excellent correlation between theoretical (920.0 mAh g^{-1}) and experimental capacities (912.1 mAh g^{-1}). Based on such Na^+ storage mechanism, it can be determined that HEP contributes 40% to the capacity in BTA-CHF, while benzothiadiazole and alkyne active sites contribute 20% and 40%, respectively.

3 | Conclusions

In conclusion, this work proposes a "three-in-one" multi-function modulation strategy to construct novel CNs with tailored electronic structures for high-performance SIBs, and develop a benzothiadiazole cooperated with alkynyl co-regulated covalent heptazine framework (BTA-CHF) as the first proof-of-concept. In BTA-CHF, the alkynyl units serve as π-electron-bridge to connect active benzothiadiazole and heptazine motifs, and thereby creating electron conduction network across the entire periodic

framework. Transcending CNs like g-C_3N_4, BTA-CHF features stronger conjugation depth, multi-redox active centers, and in particular unparalleled intrinsic electronic structure. These attributes collectively contribute to its superior conductivity and comprehensive Na^+-storage performance. Benefited from these virtues, BTA-CHF as a SIBs electrode manifested an unprecedented performance of superior reversible capacity (912.1 mAh g^{-1}/0.1 A g^{-1}), excellent rate capability (273.8 mAh g^{-1}/10.0 A g^{-1}), and heartening cyclability with less than 7% decay undergoing 20 000-cycles under 10.0 A g^{-1}. More impressively, the BTA-CHF//$Na_3V_2(PO_4)_3$ full battery exhibits a notable reversible capacity of 836.8 mAh g^{-1} at 0.1 A g^{-1}, remarkable high-rate performance of 166.9 mAh g^{-1} at 10 A g^{-1}, and maintains a high capacity of 143.2 mAh g^{-1} after 1000 cycles at 10 A g^{-1}. These results underscore the significance of creating CNs with enhanced conductivity and efficient redox activity. This work renders an attractive design paradigm for high-performance CNs in SIBs and meanwhile will expand the family of electrode materials relied on redox-active motifs.

4 | Experimental Section

4.1 | Preparation of BTA-CHF

BTA-CHF was synthesized via the Sonogashira coupling reaction under Ar atmosphere. In an usual procedure, CuI (1.0 mg) and $Pd(PPh_3)_4$ (6.0 mg) were sonicated in N,N-dimethylformamide (DMF, 2.5 mL) 10 min to obtain homogeneous dispersion. Subsequently, this mixture was added dropwise into a dispersion consisting of 55.0 mg of HEP-Cl_3 (0.2 mmol) and 55.3 mg of DT-BTD (0.3 mmol) in 2.5 mL of DMF and 5.0 mL of triethylamine in a 50-mL thick glass bottle. After sealing, the mixture maintained slight stirring at 80°C under oil bath for 48 h. After cooling to 25°C, the generated black precipitate was isolated via centrifugation and washed extensive by methanol and dichloromethane (CH_2Cl_2). To further remove residual solvents and possible by-products in the pore structure for achieving pure products, the crude product was purified through Soxhlet extraction in CH_2Cl_2 for 24 h. After vacuum drying (60°C) overnight, the final product was yielded as a black powder.

4.2 | Electrochemical Measurements

The working electrode were first prepared through homogenizing BTA-CHF, ketjen black, and polyvinylidene fluoride (PVDF) (6:2:2, weight ratio) in N-methylpyrrolidone. After homogeneous finishing this slurry on copper foil and vacuum drying (65°C, 14 h), the film was cut to the CR2032 coin cell compatible size with 1.0–1.2 mg cm^2 material loading. The prepared working electrodes were paired with sodium metal and assembled into CR2032 coin cells in an argon-atmosphere glove box with a insignificant H_2O/O_2 value below 0.1 ppm and a pressure at 1 atm. $NaClO_4$ (1.0 M) in the mixture of dimethyl carbonate and ethylene carbonate (1/1, Vol%) containing 5 wt.% floroethylene carbonate was utilized as the electrolyte. The separator was a Whatman glass microfiber filers (Φ 14 mm). The tests of rate and cycling performance, GITT analysis were conducted on Wuhan LAND CT3001A system with 0.01–3.0 V. It needs to be noted there were six activation cycles at 0.1 A g^{-1} prior to long-life testing at 10 A g^{-1}, which aimed to avoid the instability of initial cycles under this high current density. EIS (0.01 Hz–100 kHz) and CV (0.1–1.0 mV s^{-1}, 0.01–3.0 V) tests were implemented on an electrochemical workstation (BIO-LOGIC VMP3). Before assembling the full battery, $Na_3V_2(PO_4)_3$ cathode as well as BTA-CHF anode was pre-cycled in half cells, and then paired in coin cells with the mass ratio of 3.25 (the N/P ratio was about 1.1). The full battery was tested in the voltage window ranged from 0.8 to 3.6 V.

4.3 | Statistical Analysis

Quantitative data analysis followed rigorous principles to ensure reproducibility. For data pre-processing, representative results from materials characterization (e.g., FT-IR, PXRD) are shown. Raw electrochemical data from independent cell tests were used directly. Clear outliers from failed cells were excluded. Data are presented as the stable mean for electrochemical metrics (capacity, efficiency). Representative plots (CV and charge/discharge curves) at least three replicates and representative SEM/HR-TEM images from multiple regions are shown. The sample size (n) refers to independently fabricated cells. Key performance metrics (cycling, rate) are from $n \geq 3$ cells per condition. Ex-situ characterization (FTIR, XPS) used electrodes from ≥2 cells at identical states. Statistical calculations used OriginPro 2022. Electrochemical data were processed with the LAND test system software before analysis.

Author Contributions

Y.Y.X. proposed ideas and designed experiments, prepared materials, and wrote the rough paper. R.Y.F. and R.Y.B. were responsible for the characterization of materials and electrochemical testing. J.Q.Q. collected and analyzed data. C.H.L. revised the paper. W.S. is dedicated to mechanism studies. J.Z. revised the paper and directed the project.

Acknowledgements

The financial support was provided by Natural Science Foundation of Shandong Province (ZR2023QB090), and Science and Technology Support Plan for Youth Innovation of Colleges and Universities of Shandong Province of China (2023KJ281), National Key R&D Program of China (2017YFA0208200), National Natural Science Foundation of China (62288102, U25A20628, 22561160129, 22479074, 22475096, 21872069, 22022505, and 22169016), China Postdoctoral Science Foundation (2023M741624), the Project of State Key Laboratory of Organic Electronics and Information Displays, and NJUTP (GZR2023010016), Natural Science Foundation of Jiangsu Province (BK20210601, BK20240400 and BK20241236), the Science and Technology Major Project of Jiangsu Province (BG2024013), the Scientific and Technological Achievements Transformation Special Fund of Jiangsu Province (BA2023037), the Academic Degree and Postgraduate Education Reforming Project of Jiangsu Province (JGKT24_C001), the Key Core Technology Open Competition Project of Suzhou City (SYG2024122), the Open Research Fund of Suzhou Laboratory (SZLAB-1308-2024-TS005), and the Chenzhou National Sustainable Development Agenda Innovation Demonstration Zone Provincial Special Project (2023sfq11), and Natural Science Foundation of NJUPT (NY223079, NY224119), Open Fund of Key Laboratory of Functional Molecular Solids of Ministry of Education (FMS2025009).

Conflicts of Interest

The authors declare no conflict of interest.

Data Availability Statement

The data that support the findings of this study are available in the supplementary material of this article.

References

1. J. Chu, Z. Liu, J. Yu, H. Wang, F. Cui, and G.-S. Zhu, "Electronic Band Structure Engineering of π-d Conjugated Metal-Organic Framework for Sodium Organic Batteries," *Nature Communications* 16 (2025): 3549, https://doi.org/10.1038/s41467-025-58759-6.

2. J. Yu, X. Zhang, Y. Liu, et al., "Donor-Acceptor Porous Aromatic Framework Cathode with Fast Redox Kinetics for Ultralow-Temperature (-70 °C) Potassium-Organic Batteries," *Angewandte Chemie International Edition* 64 (2025): 202507570.

3. X. Qiu, X. Wang, Y. He, et al., "Superstructured Mesocrystals Through Multiple Inherent Molecular Interactions for Highly Reversible Sodium Ion Batteries," *Science Advances* 7 (2021): abh3482, https://doi.org/10.1126/sciadv.abh3482.

4. L. Chen, L. Cheng, J. Yu, et al., "Tailored Organic Cathode Material with Multi-Active Site and Compatible Groups for Stable Quasi-Solid-State Lithium-Organic Batteries," *Advanced Functional Materials* 32 (2022): 2209848, https://doi.org/10.1002/adfm.202209848.

5. Y. Wang, H. Li, S. Chen, et al., "An Ultralong-Life SnS-Based Anode Through Phosphate-Induced Structural Regulation for High-Performance Sodium Ion Batteries," *Science Bulletin* 67 (2022): 2085–2095, https://doi.org/10.1016/j.scib.2022.09.021.

6. N. Yabuuchi, M. Kajiyama, J. Iwatate, et al., "P2-Type $Na_x[Fe_{1/2}Mn_{1/2}]O_2$ Made From Earth-Abundant Elements for Rechargeable Na Batteries," *Nature Materials* 11 (2012): 512–517, https://doi.org/10.1038/nmat3309.

7. Y. Liu, N. Zhang, F. Wang, X. Liu, L. Jiao, and L. Fan, "Approaching the Downsizing Limit of Maricite NaFePO 4 Toward High-Performance Cathode for Sodium-Ion Batteries," *Advanced Functional Materials* 28 (2018): 1801917, https://doi.org/10.1002/adfm.201801917.

8. F. Xie, L. Zhang, M. Jaronies, and S.-Z. Qiao, "Na_2 Ti_3O_7@N-Doped Carbon Hollow Spheres for Sodium-Ion Batteries with Excellent Rate Performance," *Advanced Materials* 29 (2017): 1700989, https://doi.org/10.1002/adma.201700989.

9. X. Yang, L. Cong, X. Liu, et al., "Mesoporous Polyimide-Linked Covalent Organic Framework with Multiple Redox-Active Sites for High-Performance Cathodic Li Storage," *Angewandte Chemie International Edition* 61 (2022): 202207043, https://doi.org/10.1002/anie.202207043.

10. Y. Park, D. S. Shin, S. H. Woo, et al., "Sodium Terephthalate as an Organic Anode Material for Sodium Ion Batteries," *Advanced Materials* 24 (2012): 3562–3567, https://doi.org/10.1002/adma.201201205.

11. Y. Zhu, Y. Xiao, S. Sou, Y. Kang, and S. Chou, "Spinel/Post-Spinel Engineering on Layered Oxide Cathodes for Sodium-Ion Batteries," *eScience* 1 (2021): 13–27, https://doi.org/10.1016/j.esci.2021.10.003.

12. H. Zhao, J. Wang, Y. Zheng, et al., "Organic Thiocarboxylate Electrodes for a Room-Temperature Sodium-Ion Battery Delivering an Ultrahigh Capacity," *Angewandte Chemie International Edition* 56 (2017): 15334–15338, https://doi.org/10.1002/anie.201708960.

13. L. Cheng, X. Yan, J. Yu, et al., "Redox-Bipolar Covalent Organic Framework Cathode for Advanced Sodium-Organic Batteries," *Advanced Materials* 37 (2025): 2411625, https://doi.org/10.1002/adma.202411625.

14. Y. Chen, G. Zhang, M. Zou, et al., "The Role of by-Products in Proton Storage," *Chem* 10 (2024): 3656–3666, https://doi.org/10.1016/j.chempr.2024.07.039.

15. S. Yang, J. Wu, Z. Shan, et al., "Truxenone-Based Covalent Organic Framework/Carbon Nanotube Composite for High-Performance Low-Temperature Sodium-Ion Batteries," *Angewandte Chemie International Edition* 64 (2025): 202511714, https://doi.org/10.1002/anie.202511714.

16. Z. Hu, Q. Liu, S. Chou, and S. Dou, "Advances and Challenges in Metal Sulfides/Selenides for Next-Generation Rechargeable Sodium-Ion Batteries," *Advanced Materials* 29 (2017): 1700605.

17. D. Adekoya, S. Qian, X. Gu, et al., "DFT-Guided Design and Fabrication of Carbon-Nitride-Based Materials for Energy Storage Devices: A Review," *Nano-Micro Letters* 13 (2021): 13, https://doi.org/10.1007/s40820-020-00522-1.

18. G. Li, S. Guo, B. Xiang, et al., "Recent Advances and Perspectives of Microsized Alloying-Type Porous Anode Materials in High-Performance Li- and Na-Ion Batteries," *Energy Materials* 2 (2022): 200020, https://doi.org/10.20517/energymater.2022.24.

19. C. Lu and X. Chen, "Nanostructure Engineering of Graphitic Carbon Nitride for Electrochemical Applications," *ACS Nano* 2021, 15, 18777–19793.

20. Y. Wang, H. Li, B. Zhai, et al., "Highly Crystalline Poly(heptazine imide)-Based Carbonaceous Anodes for Ultralong Lifespan and Low-Temperature Sodium-Ion Batteries," *ACS Nano* 18 (2024): 3456–3467, https://doi.org/10.1021/acsnano.3c10779.

21. J. Xu, M. Wang, N. P. Wickramaratne, M. Jaroniec, S. Dou, and L. Dai, "High-Performance Sodium Ion Batteries Based on a 3D Anode From Nitrogen-Doped Graphene Foams," *Advanced Materials* 27 (2015): 2042–2048, https://doi.org/10.1002/adma.201405370.

22. X. Yang, J. Peng, and L. Zhao, "Insights on Advanced g-C_3N_4 in Energy Storage: Applications, Challenges, and Future," *Carbon Energy* 6 (2024): 490.

23. D. Adekoya, X. Gu, M. Rudge, et al., "Carbon Nitride Nanofibres with Exceptional Lithium Storage Capacity: From Theoretical Prediction to Experimental Implementation," *Advanced Functional Materials* 28 (2018): 1803972, https://doi.org/10.1002/adfm.201803972.

24. G. M. Veith, L. Baggetto, L. A. Adamczyk, et al., "Electrochemical and Solid-State Lithiation of Graphitic C_3N_4," *Chemistry of Materials* 25 (2013): 503–508, https://doi.org/10.1021/cm303870x.

25. G. Wang, Y. Xie, H. Wang, et al., "A Promising Carbon/g-C_3N_4 Composite Negative Electrode for a Long-Life Sodium-Ion Battery," *Angewandte Chemie* 131 (2019): 13865–13871, https://doi.org/10.1002/ange.201905803.

26. C. Xu, W. Yang, G. Ma, et al., "Edge-Nitrogen Enriched Porous Carbon Nanosheets Anodes with Enlarged Interlayer Distance for Fast Charging Sodium-Ion Batteries," *Small* 18 (2022): 2204375, https://doi.org/10.1002/smll.202204375.

27. X. Zhang, K. Wang, J. Qiu, et al., "Low Cobalt Single Atoms Loading on N-Doped Carbon for High Na Storage Performance," *Nano Energy* 129 (2024): 110018, https://doi.org/10.1016/j.nanoen.2024.110018.

28. G. Liu, H. Yuan, Z. Wang, et al., "Cu Single Atoms Regulating Nitrogen Active-Sites of g-C_3N_4 for Sodium Ion Storage," *Energy Storage Materials* 71 (2024): 10368, https://doi.org/10.1016/j.ensm.2024.103608.

29. X. Pan, B. Xi, H. Li, et al., "Molybdenum Oxynitride Atomic Nanoclusters Bonded in Nanosheets of N-Doped Carbon Hierarchical Microspheres for Efficient Sodium Storage," *Nano-Micro Letters* 14 (2022): 163, https://doi.org/10.1007/s40820-022-00893-7.

30. Q. Wang, G. Li, X. Feng, K. Nielsch, D. Golberg, and O. G. Schmidt, "Electronic and Optical Properties of 2D Materials Constructed from Light Atoms," *Advanced Materials* 30 (2018): 1801600.

31. M. Ruby-Raj, J. Yun, D. K. Son, and G. Lee, "Extraordinary Ultrahigh-Capacity and Long Cycle Life Lithium-Ion Batteries Enabled by Graphitic Carbon Nitride-Perylene Polyimide Composites," *Energy & Environmental Materials* 6 (2023): 12553, https://doi.org/10.1002/eem2.12553.

32. J. Liu, Y. Zhang, L. Zhang, F. Xie, A. Vasileff, and S. Qiao, "Graphitic Carbon Nitride (g-C_3N_4)-Derived N-Rich Graphene with Tuneable Interlayer Distance as a High-Rate Anode for Sodium-Ion Batteries," *Advanced Materials* 31 (2019): 1901261, https://doi.org/10.1002/adma.201901261.

33. P. Li, Y. Shen, X. Li, W. Huang, and X. Lu, "Fullerene-Intercalated Graphitic Carbon Nitride as a High-Performance Anode Material for

Sodium-Ion Batteries," *Energy & Environmental Materials* 5 (2022): 608–616, https://doi.org/10.1002/eem2.12200.

34. Z. Ye, S. Xie, Z. Cao, et al., "High-Rate Aqueous Zinc-Organic Battery Achieved by Lowering HOMO/LUMO of Organic Cathode," *Energy Storage Materials* 37 (2021): 378–386, https://doi.org/10.1016/j.ensm.2021.02.022.

35. W. Li, H. Wu, H. Zhang, et al., "Tuning Electron Delocalization of Hydrogen-Bonded Organic Framework Cathode for High-Performance Zinc-Organic Batteries," *Nature Communications* 14 (2023): 5235.

36. C. Li, W. Zhao, G. Long, Q. Zhang, S. Mei, and C.-J. Yao, "Extending the π-Conjugation of a Donor-Acceptor Covalent Organic Framework for High-Rate and High-Capacity Lithium-Ion Batteries," *Angewandte Chemie International Edition* 63 (2024): 202409421, https://doi.org/10.1002/anie.202409421.

37. S. Fu, X. Li, G. Wen, et al., "Dimensional Evolution of Charge Mobility and Porosity in Covalent Organic Frameworks," *Nature Communications* 16 (2025): 2219, https://doi.org/10.1038/s41467-025-57436-y.

38. Y. Zheng, T. Qian, H. Ji, et al., "Accelerating Ion Dynamics Under Cryogenic Conditions by the Amorphization of Crystalline Cathodes," *Advanced Materials* 33 (2021): 2102634.

39. W. Li, H. Ma, W. Tang, et al., "Single Organic Electrode for Multi-System Dual-Ion Symmetric Batteries," *Nature Communications* 15 (2024): 9533, https://doi.org/10.1038/s41467-024-53803-3.

40. S. Muench, A. Wild, C. Friebe, B. Häupler, T. Janoschka, and I. S. Schubert, "Polymer-Based Organic Batteries," *Chemical Reviews* 116 (2016): 9438–9484.

41. D. Li, X. Ren, Q. Ai, et al., "Facile Fabrication of Nitrogen-Doped Porous Carbon as Superior Anode Material for Potassium-Ion Batteries," *Advanced Energy Materials* 8 (2018): 1802386.

Supporting Information

Additional supporting information can be found online in the Supporting Information section.

Supporting File: adfm73937-sup-0001-SuppMat.docx.